Water Resources Research

RESEARCH ARTICLE
10.1029/2021WR030870

Anchoring Multi-Scale Models to Micron-Scale Imaging of Multiphase Flow in Rocks

Shan Wang[1,2], Leonardo C. Ruspini[3], Pål-Eric Øren[3], Stefanie Van Offenwert[1,2], and Tom Bultreys[1,2]

[1]Pore-Scale Processes in Geomaterials Research (PProGRess), Department of Geology, Ghent University, Ghent, Belgium, [2]Centre for X-ray Tomography (UGCT), Ghent University, Ghent, Belgium, [3]Petricore Norway A.S., Trondheim, Norway

Key Points:

- Improved differential imaging technique is used to quantify porosity and saturation distribution of a heterogeneous rock sample
- A new sub-rock typing method based on the drainage experiment is presented
- Segmentation of microporous regions plays an important role in multiphase flow simulation

Supporting Information:

Supporting Information may be found in the online version of this article.

Correspondence to:

S. Wang,
Shan.Wang@UGent.be

Citation:

Wang, S., Ruspini, L. C., Øren, P.-E., Van Offenwert, S., & Bultreys, T. (2022). Anchoring multi-scale models to micron-scale imaging of multiphase flow in rocks. *Water Resources Research*, *58*, e2021WR030870. https://doi.org/10.1029/2021WR030870

Received 20 JUL 2021
Accepted 31 DEC 2021

Abstract Image-based pore-scale modeling is an important method to study multiphase flow in permeable rocks. However, in many rocks, the pore size distribution is so wide that it cannot be resolved in a single pore-space image, typically acquired using micro-computed tomography (micro-CT). Recent multi-scale models therefore incorporate sub-voxel porosity maps, created by differential micro-CT imaging of a contrast fluid in the pores. These maps delineate different microporous flow zones in the model, which must be assigned petrophysical properties as input. The uncertainty on the pore scale physics in these models is therefore heightened by uncertainties on the representation of unresolved pores, also called sub-rock typing. Here, we address this by validating a multi-scale pore network model using a drainage experiment imaged with differential micro-CT on an Estaillades limestone sample. We find that porosity map-based sub-rock typing was unable to match the micrometer-scale experimental fluid distributions. To investigate why, we introduce a novel baseline sub-rock typing method, based on a 3D map of the experimental capillary pressure function. By incorporating this data, we successfully remove most of the sub-rock typing uncertainty from the model, obtaining a close fit to the experimental fluid distributions. Comparison between the two methods shows that in this sample, the porosity map is poorly correlated to the multiphase flow behavior of microporosity. The method introduced in this paper can help to constrain the sources of uncertainties in multi-scale models in reference cases, facilitating the development of simulations in complex reservoir rocks important for for example, geological storage of CO_2.

Plain Language Summary Understanding multiphase flow within heterogeneous reservoir rocks is crucial for geological reservoir management. These rocks usually have intricate microstructures (unresolved or sub-resolution pores) which are difficult to quantify. Pore-scale modeling combined with imaged-based experiments can be a useful tool to describe complex pore structures, which is of key importance in the subsequent simulation and prediction of multiphase flow behavior. In this study, we focus on improving the representation of unresolved porous regions of a heterogeneous rock sample (also called sub-rock typing). A drainage experiment was performed and imaged by micro-computed tomography to characterize the multiphase distribution at increasing capillary pressures. The predictions of two multi-scale models, which were generated according to distinct sub-rock typing methods on the same sample, were compared with the drainage experimental data. We found that the model obtained by the "classical" sub-rock typing method was unable to simulate the correct arrangement of fluids in this sample, while the new method performed better, which illustrates the importance of rock type identification to pore-scale modeling. The workflow presented in this paper can be extended to create reliable reference models so that uncertainties on model input can be reduced, leading to improved simulations in complex geological materials.

1. Introduction

Multiphase flow through rocks plays an important role in numerous earth science applications, such as hydrocarbon recovery (Olayiwola & Dejam, 2019; Wang et al., 2020), carbon dioxide storage (Arif et al., 2017), remediation of polluted aquifers (Bortone et al., 2013) and subsurface energy storage in the form of hydrogen or compressed air (Amid et al., 2016; Mouli-Castillo et al., 2019). Many reservoir rocks, notably carbonates and clay-bearing sandstones, exhibit complex pore geometries with very wide pore size distributions. The petrophysical properties of such rocks often do not obey classical correlations (Prodanović et al., 2015; Shanley et al., 2004), spurring pore-scale studies of their fluid flow behavior (Mehmani et al., 2020). This can be done based on images of the pore space, obtained with for example, micro-computed tomography (micro-CT) and

(FIB-)SEM imaging (Bera et al., 2011; Bultreys, De Boever, & Cnudde, 2016; Ciobanu et al., 2011; Cnudde & Boone, 2013; Wirth, 2009).

Despite the wide interest in simulating fluid flow in complex, multi-scale pore spaces, the trade-off between image size and resolution in most imaging techniques complicates the development of suitable image-based approaches (Blunt et al., 2013). Typical imaging workflows identify resolved pores and zones with unresolved porosity (below the μm scale) in micro-CT images of mm-scale samples, which usually capture the largest pore features. Unresolved porosity is visible in these images as zones with gray values that are intermediate between solid and void, due to their intermediate density (Cnudde & Boone, 2013). These regions can then be imaged by higher-resolution techniques, that are then correlated back to the lower-resolution micro-CT scan (De Boever et al., 2015; Devarapalli et al., 2017; Lin et al., 2019). The unresolved pores, which we will by definition refer to as the microporosity, can play a crucial role in the sample's multiphase flow behavior (Bultreys, Stappen, et al., 2016; Mehmani et al., 2020). Therefore, specialized multi-scale models are required that fuse the resolved pores with information on the microporosity features, typically obtained using higher-resolution images on small sub-sections of the sample (Menke et al., 2019).

Image-based modeling is widely used to study fluid flow in complex reservoir rocks including solute transport in carbonate (Scheibe et al., 2015), gas transport in shale rock (Guo et al., 2018), two-phase flow and deformation in porous materials (Carrillo & Bourg, 2021), etc. Multi-scale models are an extension of pore-scale, image-based modeling techniques, consisting of either direct numerical simulations (Alhashmi et al., 2015; Pan et al., 2004; Raeini et al., 2012) or pore network models (PNMs; Blunt et al., 2013; Dong & Blunt, 2009). Direct numerical simulations of multiphase flow usually require large computational resources and therefore struggle to capture capillary-dominated flow on large images (Blunt et al., 2013). PNMs feature higher computational efficiencies due to simplifications on the geometry and the fluid displacement physics, which makes them well-suited for multi-scale simulations. Networks obtained at different resolutions or scales can be extrapolated in space and fused to reconstruct a multi-scale pore network (Jiang et al., 2013; Mehmani & Prodanović, 2014), resulting in detailed but very large networks. Alternatively, the micropores can be treated as a continuous porous medium with specific petrophysical properties to reduce the size of the network while still representing the connectivity caused by microporosity (Bauer et al., 2012; Bultreys et al., 2015; Youssef et al., 2008).

Despite the progress in representing multi-scale pore networks, it remains difficult to assess the model uncertainties. Multi-scale pore network models depend on a significant amount of uncertain input information to describe the microporosity behavior, which complicates the validation of the physical assumptions in the model itself (e.g., quasi-static fluid displacement). An important aspect of the input uncertainty is that only a limited volume of microporosity is typically imaged at the highest resolutions, while there is often significant heterogeneity in its properties. Recent approaches have addressed this information gap by incorporating sub-voxel porosity maps (Ruspini et al., 2016, 2021). The porosity map can be generated based on differential imaging: measuring the calibrated gray value change when the pore space is filled with a high-contrast fluid such as high-concentration potassium iodide or cesium chloride (Boone et al., 2014; Ghous et al., 2007; Lin et al., 2016). The resulting map is then used for "sub-rock typing": identifying and characterizing zones with different microporosity properties in the model. The common approach is to perform a segmentation on dry images or differential images directly to separate distinct phases, sometimes followed by a series of image processing operations to alleviate artifacts at phase boundaries (Bauer et al., 2012; Bultreys et al., 2015). However, there is still a lack of validation to reveal whether these approaches can provide a reasonable representation for unresolved pores and how much uncertainty they introduce into the multi-scale PNM simulations.

Recent work on single-scale pore network models has illustrated how pore-by-pore validation of the fluid distributions during drainage or imbibition can serve to study model uncertainties (Bultreys et al., 2018, 2020; Øren et al., 2019). A similar principle used to generate porosity maps can be used to track the fluid saturation in microporous regions during multiphase flow experiments (Gao et al., 2017; Lin et al., 2016). In this paper, we propose a pore-by-pore comparison of fluid distributions for multi-scale PNM by comparing fluid distributions in the model to a differential micro-computed tomography (micro-CT) based drainage experiment on a heterogeneous Estaillades limestone (as shown in Figure 1). Using this data, we validate the porosity-map based workflow, and explain its uncertainties by comparing to a novel data-based model, which takes its microporosity information from the micro-CT drainage experiment. The experiment and the image processing workflows are introduced in Section 2.1. Then, the multiscale PNM workflow including the two sub-rock typing methodologies

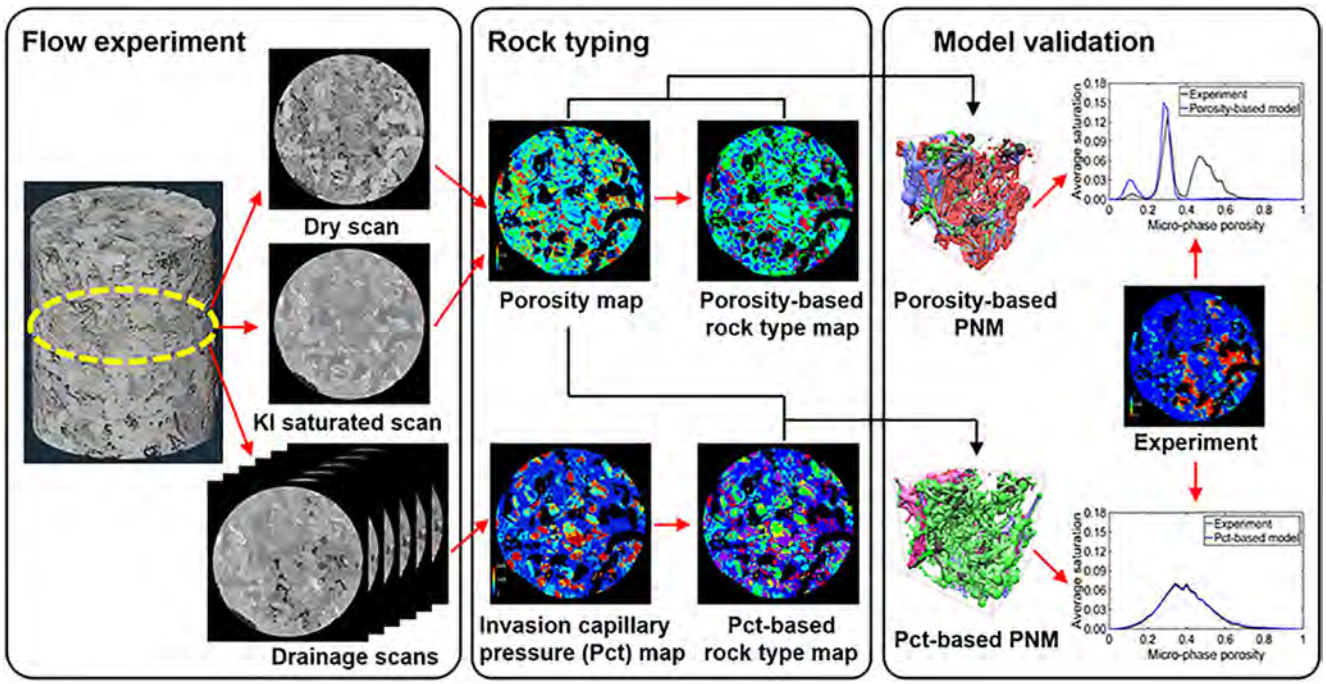

Figure 1. The validation workflow for multi-scale pore network model.

(porosity-based and drainage-based methods) are explained in Section 2.2. In Section 3, we compare the predictions from the two models with experimental data and discuss the reasons that may lead to simulation uncertainties. Section 4 discusses the conclusion and the outlook for our future research.

2. Materials and Methods

2.1. Experiment

The main goal of the experiment presented here is to measure the brine and decane distribution within both macropores and microporous regions of the sample during capillary drainage. In the following, the sample and fluid preparation, the set-up, the experimental procedure and data processing workflow will be discussed in detail.

2.1.1. Rock Samples and Fluid Preparation

The rock sample used in the experiment is Estaillades limestone, which has a complex pore structure featuring a bi-modal pore size distribution. The broad pore size distribution has two peaks with modes of respectively 390 nm and 19 μm (Han et al., 2007). Estaillades limestone is composed of 99% calcite (Alyafei & Blunt, 2016). A sample with a diameter of 6 mm and a length of 20 mm was cored and vacuum-saturated with deionized water to ensure that all the air was removed from the pores before the experiment.

As fluid phases in the drainage experiment, we used KI-brine and decane. The former acted as wetting phase, while the latter was the non-wetting phase. The brine was made from deionized water doped with 25 wt% potassium iodine (KI) as a contrast agent due to its high X-ray attenuation coefficient. This solution provided a strong contrast to identify the fluid phases in the micro-CT images.

2.1.2. Drainage Experiment

The experimental apparatus and flow lines are shown in Figure 2. The rock sample was placed on top of a water-wet ceramic porous plate (Cobra Technologies B.V., NL) and then wrapped in a Viton sleeve. The hydrophilic porous plate had an invasion pressure of 1,300 kPa to prevent early breakthrough of the non-wetting phase. This assembly was placed in an X-ray transparent flow cell made out of PEEK (RS Systems, Norway), connected to high-precision syringe pumps supplying the experimental fluids. A differential pressure transducer (Keller PD-33X) was connected to the inlet and outlet of the sample. The flow cell was then placed on the Environmental

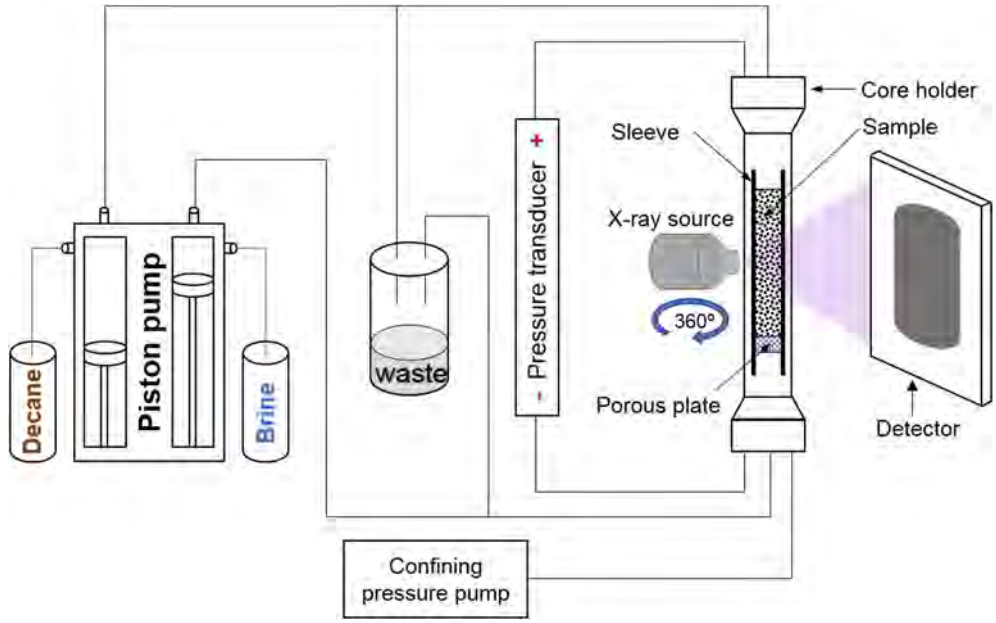

Figure 2. Experimental apparatus used in the drainage experiment.

Micro-CT (EMCT) scanner at Ghent University's Centre for X-ray Tomography (UGCT; Bultreys, Boone, et al., 2016; Dierick et al., 2014). This scanner consists of a rotating source-and-detector gantry, meaning the flow cell remained static during the full experiment. Throughout the experiment, the X-ray beam was filtered with 1 mm aluminium to reduce the beam hardening effect. The experiment was performed by executing the following steps:

1. A confining pressure of 3,500 kPa was set to compress the Viton sleeve, to avoid fluid bypassing along the wall of sample.
2. The water-saturated sample was scanned by micro-CT at room temperature and pressure. The imaging settings were: 6.5 µm voxel size, 2,400 projections, 1,150 ms integration time per radiograph; 110 kV and 8 W X-ray tube settings. Since water has a low gray value similar to air in the images, we will refer to this as the "dry scan" or "dry image" in following sections for convenience.
3. The water was flushed out by brine, which was injected through the sample with a maximum flow rate of 0.075 ml/min for 4 hr and left overnight. A high-quality micro-CT scan was conducted to capture the sample's 100% brine saturated state (same imaging settings as step 2).
4. The drainage was started by injecting decane from the top of the flow cell at a low flow rate (0.001 ml/min). To set a constant pressure drop over the sample, which at vanishing flow rates yields a set capillary pressure in the sample, the flow rate was subsequently gradually lowered based on manual inspection of the pressure transducer reading. This proved to be more reliable than using automated constant-pressure settings on the syringe pump, particularly at low set pressures. The experiment remained capillary dominated at all times during this equilibration procedure, as the maximum capillary number was 6.2×10^{-8}.
5. Radiographs of the sample were collected and subtracted from each other to track the saturation change in the sample during the equilibration (Figure S1 in the Supporting Information S1). In addition, a short micro-CT scan (6.5 µm voxel size, 2,400 projections, 115 ms exposure time) was performed every hour to further compare flow distribution changes. When no more changes were found from both the differential radiographs and the subsequent micro-CT images at the target pressure, a high-quality scan (imaging settings see step 2) was taken.
6. Steps 4 and 5 were repeated with gradually increasing pressure. We performed six capillary pressure steps during the experiment, at 8, 14, 80, 180, 220 and 400 kPa. Equilibration took between 4 and 7 hr for the different pressure steps, in all cases having reached very low final flow rates (below 0.0003 ml/min).

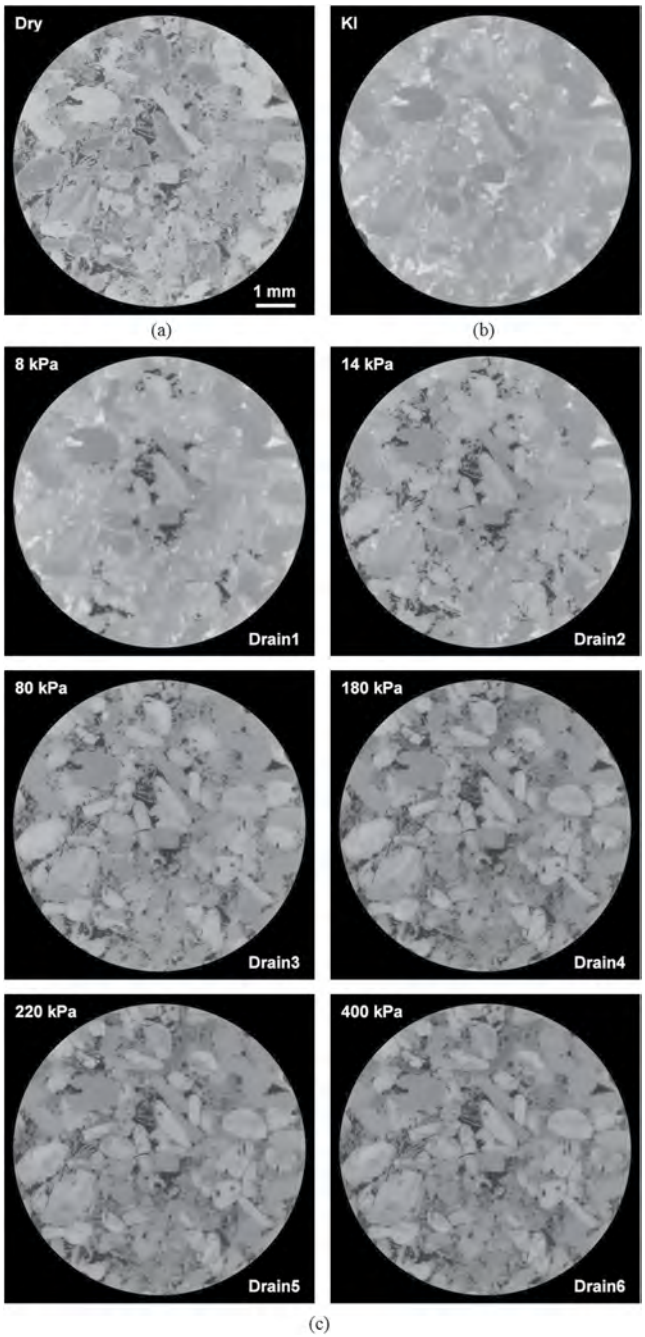

Figure 3. (a) Dry san. (b) potassium iodine saturated scan. (c) Drainage scans at six capillary pressures.

2.1.3. Micro-CT Image Processing

The acquired tomograms, which represent the 3D distribution of X-ray attenuation coefficients in the sample, were reconstructed using Octopus Reconstruction software (Tescan-XRE, Belgium). After reconstruction, the image processing was performed using Avizo 2020.2 (ThermoFisher, France). The brine-saturated and drainage-step images were all registered to the dry image using normalized mutual information and resampled using the Lanczos algorithm to make sure all the images are aligned in space. The images were then filtered with a non-local means edge-preserving filter to reduce the image noise. As shown in Figure 3, the pores in the dry scan image are dark gray and have significantly lower gray values than solid calcite grains. In the brine-saturated image, the brine-invaded pores are brighter than other phases in the sample. A cross-section of the fluid distribution in the six capillary pressure steps is shown in Figure 3c. With the increase of drainage pressure, the brine is displaced by decane, and brighter pores gradually become "black."

Although the KI-brine visually already indicates the presence of different fluid phases within macropores, further processing is necessary to quantify the brine saturation in the unresolved porosity. We propose an improved workflow here based on differential imaging with normalized deionized-water-filled and contrast-brine-filled images to calculate the sub-resolution saturation in voxels that contain microporosity. The deionized-water-image serves the same function as a dry scan in other studies (e.g., Lin et al., 2016), but has the advantage that the sample could be vacuum-saturated outside of the flow cell prior to the experiment (see Section 2.1.2). For convenience we will further refer to this scan as the "dry scan."

The image normalization is based on selecting fixed gray values for two known materials, setting them to the same value in the different images, and doing a linear rescaling of everything in between. To normalize the brine-saturated image to the dry image, we first manually selected three region-of-interests (ROI) of solid grain to determine the upper normalization value, and an ROI in the sleeve (which has a low gray value) for the lower value. The rescaled image was calculated following Equation 1, which is adapted from Lin et al. (2017):

$$I_{\text{new}} = (I - p_{\text{s\_brine}}) \cdot \frac{p_{\text{g\_dry}} - p_{\text{s\_dry}}}{p_{\text{g\_brine}} - p_{\text{s\_brine}}} + p_{\text{s\_dry}} \quad (1)$$

where I_{new} is the rescaled image, I is the image before normalization, $p_{\text{g\_dry}}$ is the average mode of the three solid grain ROIs from the dry image, $p_{\text{s\_dry}}$ is the mode of the gray value histogram of the sleeve ROI from the dry image, $p_{\text{g\_brine}}$ is the average mode of the three solid grain ROIs from the brine saturated image, and $p_{\text{s\_brine}}$ is the mode of the sleeve ROI from the brine saturated image.

For the drainage images, we first cropped three ROIs in solid grains and three ROIs in water-filled resolved pores from the dry and the six drainage images, extracted their gray value histograms and calculated their modes. The drainage images were then rescaled according to Equation 2:

$$I_{\text{new}} = (I - p_{\text{d\_drain}}) \cdot \frac{p_{\text{g\_dry}} - p_{\text{w\_dry}}}{p_{\text{g\_drain}} - p_{\text{d\_drain}}} + p_{\text{w\_dry}} \quad (2)$$

where $p_{\text{g\_dry}}$ is the average mode of three solid grain ROIs in the dry image, $p_{\text{w\_dry}}$ is the average mode of three water-invaded-pore ROIs from the dry image, $p_{\text{g\_drain}}$ is the average mode of three solid grain ROIs from the drainage images, $p_{\text{d\_drain}}$ is the average mode of three decane-invaded-pore ROIs from drainage images.

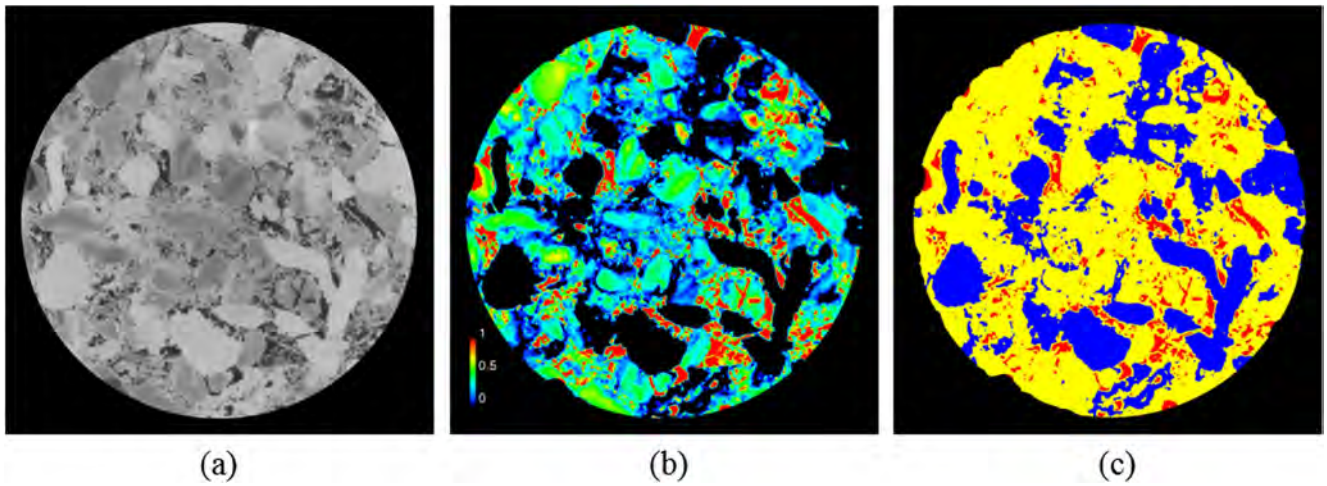

Figure 4. Porosity distribution map. (a) A slice from the filtered dry image. (b) The corresponding porosity distribution map at the same slice. (c) Three-phase segmentation of the sample into macropores (red), microporous regions (yellow) and solid (blue).

Then, the differential image was obtained by calculating the differences between the rescaled drainage- or brine saturated images and the water-filled image:

$$I_{\text{diff\_drain}} = I_{\text{new\_drain}} - I_{\text{dry}} \tag{3}$$

$$I_{\text{diff\_brine}} = I_{\text{new\_brine}} - I_{\text{dry}} \tag{4}$$

The dry-brine differential image was used to quantify sub-resolution porosity in the image, due to the assumed linear dependence of the gray value in the differential image and the volume percentage of brine present in each voxel. We denote the thresholds set for solid (0% porous) and open porosity (100% porous) voxels as CT1 and CT2, respectively. CT1 was determined based on the valley between the gray value distributions of the solid and microporous phase in the histogram. CT2 was found by masking the differential image with the macropores segmented from the dry image, and finding the peak of the associated gray value histogram (Figure S2 in the Supporting Information S1). Voxels with gray values equal to or less than CT1 are assigned 0% porosity, those equal to or higher than CT2 are assigned 100% porosity, the microporous region between CT1 and CT2 is assigned 0–100% porosity, using:

$$\varphi_{\text{micro}} = \frac{I_{\text{diff\_brine}} - CT1}{CT2 - CT1} \tag{5}$$

where φ_{micro} is the porosity within microporous voxels. The total porosity can be calculated by:

$$\varphi_{\text{total}} = \frac{V_{\text{macro}} + V_{\text{micro}} * \varphi_{\text{micro}}}{V_{\text{sample}}} \tag{6}$$

where V_{macro} is the number of macropore voxels, V_{micro} is the number of micro-pore voxels, V_{sample} is the number of voxels in the whole sample.

Similarly to the porosity map, we also calculated the brine saturation map at each capillary pressure step using Equation 7:

$$S_{\text{w\_drain}} = \frac{\varphi_{\text{drain}}}{\varphi_{\text{micro}}} = \frac{I_{\text{diff\_drain}} - CT1}{I_{\text{diff\_brine}} - CT1} \tag{7}$$

With this method, the porosity distribution map was obtained, shown in Figure 4b, which provided a 3D distribution of the porosity variation within the microporous phase. Table 1 shows the porosity calculation results. The total porosity of this sample was 25.43%, of which the sub-resolution porous regions contributed 78.53%. This is consistent with measurements (24.7%–28%) in the literature (Alyafei et al., 2015; Bauer et al., 2012; Youssef

Table 1
Porosity Calculation

Phase	Threshold	Voxel ($\times 10^8$)	Voxel × porosity ($\times 10^8$)	Average porosity	Volume fraction	Contribution	Total porosity
Macro	>1	0.42576		1	0.05463	0.05463	0.2543
Micro	0–1	5.01773	1.55637	0.31017	0.64381	0.19969	
Grain	<0	2.35033		0	0.30156	0	

et al., 2008). The three components, macropores, microporous regions and solid grains, were extracted from this porosity map (Figure 4c and Figure S3 in the Supporting Information S1).

2.2. Multi-Scale Model

2.2.1. Sub-Rock Typing

Multi-scale models of multiphase flow depend on the classification of regions with sub-resolution porosity. To identify these regions, and inform their description in the model, a recently proposed method is to segment a sub-resolution porosity map of the sample into different "sub-rock types." We will refer to this as the "porosity-based" method. A crucial first step is to generate an accurate porosity map (Figure 4b). Figure S4 in the Supporting Information S1 depicts the histogram of the porosity distribution in the sample. Two thresholds (0.2 and 0.4) were manually selected to divide the sample into three microphase regions or three rock types (3RT), based on trial-and-error to obtain realistic simulation results for the capillary pressure curve (see further). Note that this fitting approach may introduce a certain level of arbitrariness in the amount of rock types used in the model, as this also depends on the parameters assigned to each rock type. The sub-rock typing result is shown in Figure 6.

The downside of porosity-based sub-rock typing is that it is based on the assumption that porosity is closely correlated to the multiphase flow properties of the microporosity. This is not necessarily the case. Therefore, we introduce a new method here to perform rock typing based directly on experimental multiphase flow data. To this end, we determined the invasion capillary pressure (Pct) distribution within the porous phase. First, the saturation map at each drainage pressure step was calculated (Section 2.1.3). The saturation variation with the increase of pressure of every individual voxel was thus obtained. Next, these saturation maps were mean-filtered and down-sampled by a factor 2 to reduce the noise dependency and computational load. Then, a Brooks-Corey-type P_c formulation (Brooks & Corey, 1964) was fitted to the capillary pressure-saturation data points of each voxel using a least squares approach in Matlab. This yielded a relation of the following form for each voxel:

$$P_c = P_{ct}\left(\frac{1}{S_w}\right)^{\frac{1}{\lambda}} \tag{8}$$

where P_c is the capillary pressure, P_{ct} is the fitted threshold pressure (invasion capillary pressure), λ is a fitted parameter related to the pore size distribution and S_w is water saturation.

In this way, P_{ct} and λ values were derived for all porous voxels. The fitted curves for two representative voxels are shown in Figure 5a. Figure 5c presents the Pct map and the λ map, showing the 3D variation of the capillary pressure behavior in the sample. We primarily used the Pct map here due to its easier interpretability and lower noisiness than the λ-map. We considered both porosity and Pct together by performing a k-means clustering on the (φ, Pct) points of all the voxels (Figure 5b). This was used to divide the voxels into five clusters, representing five microporous subrock types, next to the macroporous and solid voxels in the image.

2.2.2. Pore Network Extraction and Simulations

Two multi-scale PNMs of the sample were extracted using the porosity map and the sub-rock type maps as input. These PNMs consist of four types of network elements: resolved nodes ("pores") and links ("throats") that represent the macroporosity and unresolved ("Darcy") nodes and links that represent the microporosity. The extraction is based on skeletonization and maximal ball clustering of the resolved pore space and each of the microporosity sub-rock types in order to find the centers of nodes and links, which reflect local dilations and constrictions in the geometry, as described in Øren et al. (2019). These are then connected together to honor the connectivity of

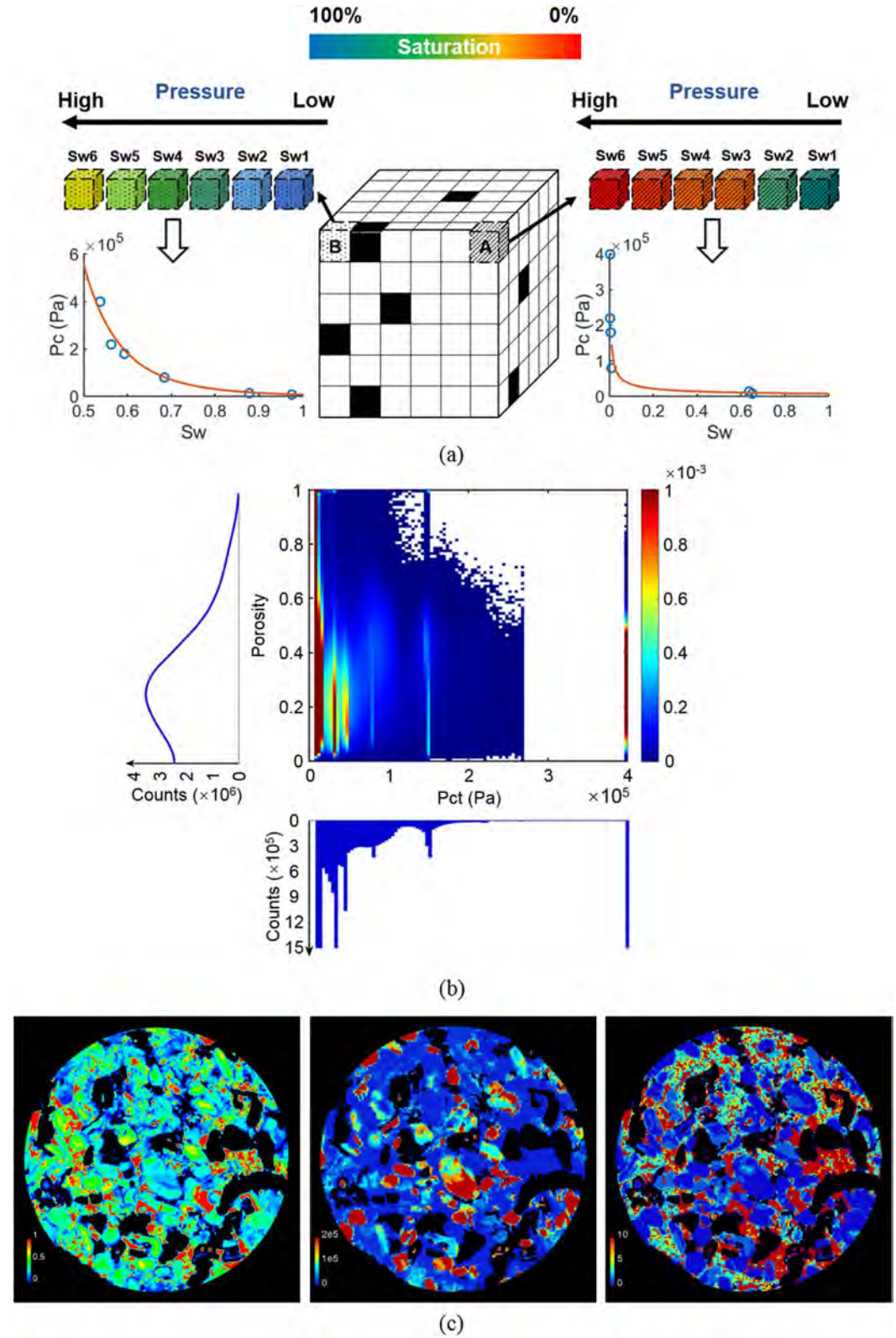

Figure 5. Pct-based sub-rock typing workflow. (a) The diagram of data fitting of two representative voxels. (b) A plot of Pct versus porosity. (c) Porosity map (left), Pct distribution map (middle) and λ distribution map (right). Note that the macropores have infinite λ and are therefore shown in red.

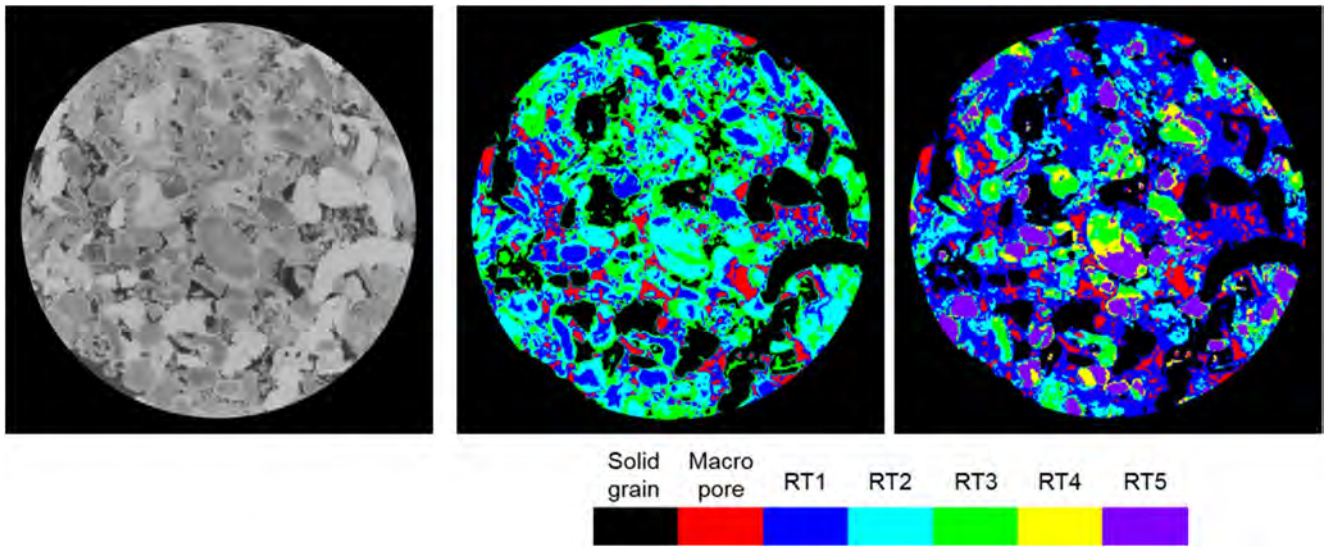

Figure 6. Dry image (left), porosity-based sub-rock typing result (middle) and Pct-based sub-rock typing result (right). The red and black in both sub-rock typing maps refer to macropores and solid grain. In porosity-based map: RT1, RT2 and RT3 show high, middle and low microporosity regions respectively. In Pct-based map: RT1 to RT5 represent lower to higher Pct microporous regions.

the multi-scale pore-space. Geometrical properties (e.g., inscribed radius, volume, shape factor) of the network elements are subsequently determined. For Darcy nodes and links, the geometrical properties are supplemented by the local porosity determined from the porosity map, and local petrophysical properties based on user input for each sub-rock type (see Section 2.2.3). Note that the sub-resolution imaging workflow may result in barely resolved pores or throats being treated as Darcy regions (Gao et al., 2019), which may lead to a poor approximation of their behavior in the model. Full details on the method can be found in Ruspini et al. (2021). We extracted two different PNMs of the same sample, based on respectively the porosity-based sub-rock typing map and the Pct-based sub-rock typing map (Figure 6). The properties of these PNMs are shown in Table 2. The total porosity was 26.2% with 5.6% contributed by macropores and 20.6% by micropores, which honors the micro-CT results (Table 1).

After extraction, the resulting PNMs were used to predict permeability and pore-scale fluid distributions during drainage. Permeabilities were calculated by assigning a conductivity value to each element (based on Poisseuille flow in resolved network elements and Darcy's law in Darcy elements, taking the local microporosity's permeability) and solving a set of mass balance equations (Ruspini et al., 2021). Drainage was simulated quasi-statically by calculating an invasion capillary pressure for each network element, and then performing an invasion-percolation (i.e., progressively invading accessible network elements in ascending order of their invasion capillary

Table 2
Properties of Extracted Pore Network Models

Properties	Porosity-based model	Pct-based model
Resolved nodes	72064	72108
Resolved links	30751	30819
Darcy nodes	594479	554739
Darcy links	4303831	4514395
Average coordination number (resolved nodes)	5.9	6.7
Average coordination number (Darcy nodes)	13.9	15.5
Total porosity	0.2625	0.2624
Resolved porosity	0.0564	0.0563
Unresolved porosity	0.2061	0.2061

pressure). Invasion capillary pressures for resolved pores and throats were calculated by assuming triangular, square or cylindrical cross-sectional shapes (Mason & Morrow, 1991). In Darcy elements, the invasion pressure was found from input capillary pressure curves of the sub-rock type (scaled according to the local porosity and permeability using the Leverett-J-curve). The simulation took fluid connectivity through wetting layers into account, and assumed a fluid to be connected through a Darcy element as long as the local relative permeability to the fluid was larger than zero. Full details are provided in Ruspini et al. (2021).

2.2.3. Petrophysical Properties

The petrophysical properties taken into account to represent unresolved porosity in each Darcy node of the PNM are porosity, permeability, relative permeability and capillary pressure curve (P_c-curve). The local porosity in each element was determined from the porosity map. Compared with the traditional way of assigning an average porosity value to the whole microporosity phase, the introduction of the porosity map captures more realistic porosity heterogeneity. The permeability for each node was calculated from a power correlation $k = a * \varphi^b$, where a and b are supplied as input values for each sub-rock type. Parameter b was set to 3.37 for all types based on a nm-scale imaging study performed by Menke et al. (2019) on microporosity in Estaillades. Since the microporosity's permeability values affect the invasion capillary pressure curve of Darcy nodes through Leverett-J scaling, parameter "a" was tuned to match the output P_c-curve of the PNM simulations with our experimental P_c-curve measurement (Section 2.1). Note that anchoring simulations to available experimental data is common practice for multi-scale models, in order to allow better predictions of more difficult-to-obtain properties.

The determination of the relative permeability curve for each rock type is a challenging task, as this property is difficult to measure directly. Here, the Brooks-Corey model (Brooks & Corey, 1966) was used to assign the same relative permeability curves to all Darcy elements, in order to decrease its uncertain influence on the drainage simulation results. Approaches to obtain more accurate relative permeability curves for different micro-regions are the subject of future investigations.

For the porosity-based PNM, the Brooks-Corey-type P_c formulation (Brooks & Corey, 1964) was fitted to the experimental Pc-measurement to obtain P_c-curves for each microporosity type. The fitted curve was split into three parts, corresponding to the three microporosity regions from the porosity map (see Section 2.2.1). The saturation range of each of these parts was then rescaled to a range between 0 and 1, to serve as input P_c-curves for the sub-rock types, where the curve with the lowest Pc-range was assigned to the rock type with the highest porosity. Note that this workflow represents a coarse fit of the input properties to the experimental Pc-data (see e.g., Bultreys et al., 2015), but that this may not generally yield good results for all samples, and that there is no set way to divide the experimental P_c-curve into the individual sections (in this work, this was done by trial-and-error, until a satisfactory fit was found between the simulated and the experimental P_c-curves).

For the Pct-based PNM, the input properties were not tuned to fit simulated output P_c-curves to experimental data, which has the danger of potentially leading to overfitting, but rather determined directly from the Pct and porosity maps. P_c-curves of each rock type were calculated directly from the imaging data, that is, the average saturation within each sub-rock type was determined at each capillary pressure step. Then, each rock type's "a" parameter in the poroperm-correlation was determined by calculating the expected permeability from these P_c-curves using the Purcell method (Purcell, 1949), and taking each rock type's average porosity ("b" values and relative permeabilities were set the same way as in the porosity-based model). The inclusion of pore-scale Pct-maps can thus significantly reduce the input uncertainty of the simulations compared to the classical workflow.

3. Results

3.1. Simulation Results

The permeability values simulated with the Pct-based model and porosity-based model were 69.51 and 9.54 mD respectively, compared to literature values of 95.5 to 283.6 mD (Alyafei et al., 2015; Bultreys et al., 2015; Nono et al., 2014) and minipermeameter values 202.4 ± 86.9 mD. The macro-porosity in the imaged sample did not percolate if the microporosity was not taken into account, and the latter thus plays an important role in the permeability calculation.

To validate the experimental workflow and the image analysis results from it, we compared the drainage results with a capillary pressure curve obtained using mercury invasion capillary pressure (MICP) method (Bultreys

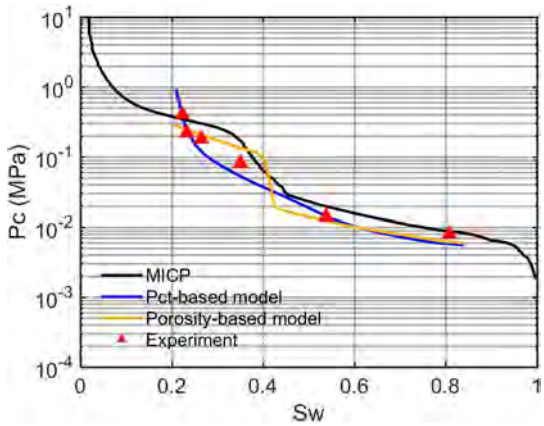

Figure 7. Comparison of capillary pressure curve obtained from Mercury Invasion Capillary Pressure experiment, our drainage experiment, and simulations.

et al., 2015), rescaled to the water-decane interfacial tension (48.3 mN/m) and contact angle (0°). As shown in Figure 7, the evolution of the saturation from the imaging with the capillary pressure imposed in our experiment agreed well with the MICP data, indicating that the experimental operation and data processing methods were reasonable and reliable. It should nevertheless be noted that the MICP experiment and the imaging experiment were performed on different samples cored from different blocks at different times, and discrepancies may thus be due to inter-sample heterogeneity. This may explain why the "bump" in the MICP curve (related to the micro-and macroporosity being connected to each other in parallel, Bultreys et al., 2015) is less pronounced in the imaged sample's P_c-curve. This is consistent with the fact that the macro-porosity did not percolate in the latter. The simulated capillary pressure curves also showed a good match with our experiment, and the input parameters were thus considered to be reasonable for the further pore-by-pore evaluation of the model.

3.2. Model Validation of Fluid Distributions

Figure 8 shows the slice-average probile of brine saturation along flow direction in the sample. Visual comparision indicates that the distribution simulated by the Pct-based model generally fits more closely to the experimental measurements.

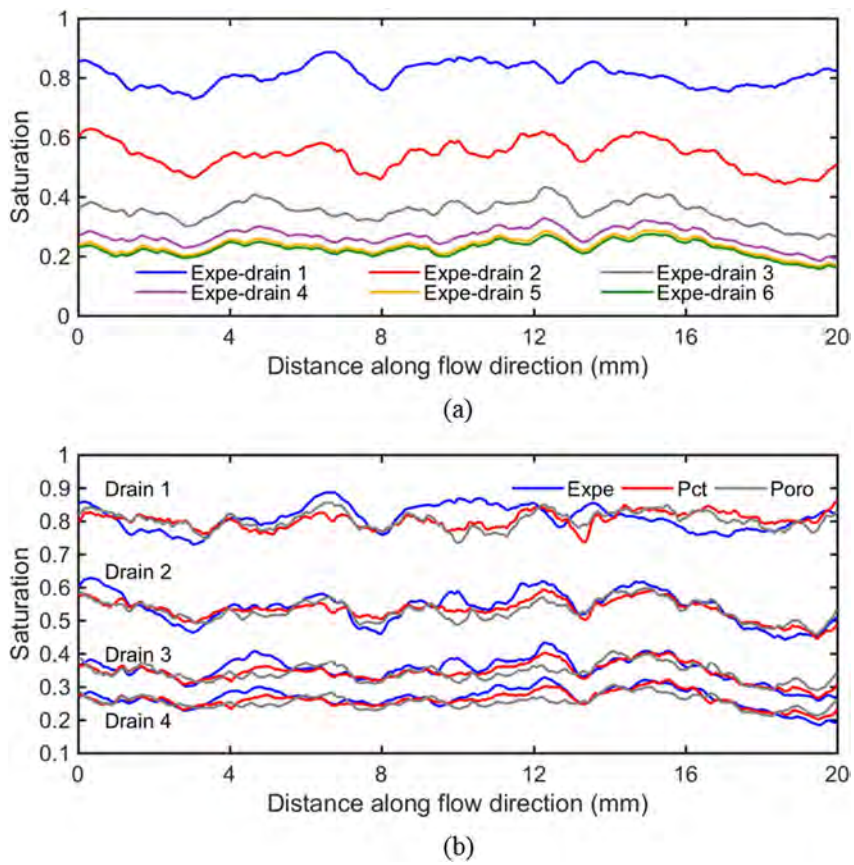

Figure 8. Brine saturation slice-average profiles along fluid flow direction. (a) Experimental results. (b) Comparison of experiment and model predictions at 1 to 4 drainage steps.

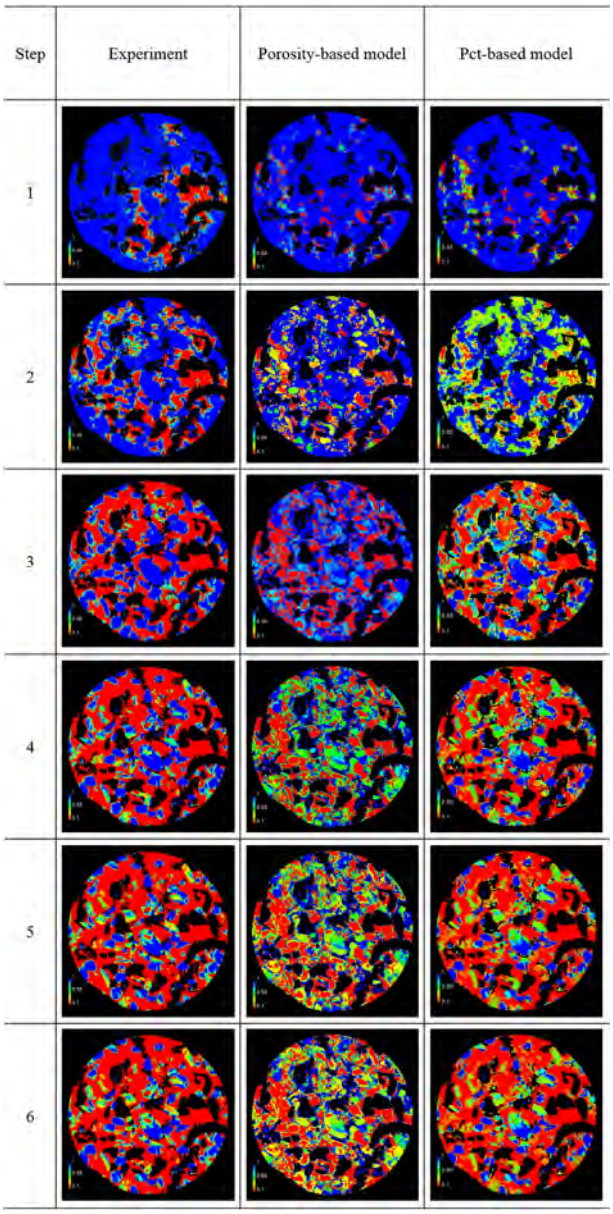

Figure 9. Saturation map comparison at each drainage pressure. The left column is experimental results. The middle and right column are simulation results in porosity-based and Pct-based pore network model.

The simulations were then compared to each step of the imaging experiment at a matching total saturation. Figure 9 shows the comparison between saturation distributions of the experiment and the two model cases. In general, the rock type segmentation was found to have an important influence on the pore scale fluid distributions, while its impact on the upscaled model outputs could be (over)compensated by tuning the petrophysical properties of the rock types. This points to the non-uniqueness of parameter assignment in the model. In the first and second drainage stage, due to the low capillary pressure, large macro pores and well connected micropores with low invasion pressures are invaded by oil, while other macro pores remain uninvaded or partially invaded. In these stages of the drainage, throats just below the resolution that connect the larger pores may cause errors: their invasion capillary pressures are treated as if they are Darcy regions, which may yield pore estimates. From the third capillary pressure on, the displacement takes place almost completely in the microporous regions. This general trend was captured by both models. However, visual inspection of the fluid saturation maps shows that the new Pct-based model performs significantly better than the classical porosity-based model in predicting the fluid distribution.

The observed discrepancy in the porosity-based model is related to the fact that the porosity-based model (similarly to most classical multi-scale models) assumes that regions with higher porosity have larger pore sizes and are more easily drained. Contrary to this classical assumption, the experiment shows that the sub-rock type with the lowest average porosity has the lowest water saturation at high capillary pressure steps (Figure 10). While the model contained enough degrees of freedom for it to be tuned to the sample-averaged capillary pressure curve in Figure 7, this is not the case for the pore-scale distribution of the fluids. Matching this distribution is known to be a crucial issue to obtain reliable relative permeability curves from the model (Bultreys et al., 2020; Gharbi & Blunt, 2012; Ruspini et al., 2017). Comparison to the novel Pct-based method, which is directly based on the invasion pressure of each pore and provides a much better match, shows that the fluid distribution discrepancy can be resolved by avoiding the basic assumption that higher porosities are related to lower invasion capillary pressures in the sub-rock typing.

3.3. Saturation Error

To investigate the accuracy of the predicted saturations further, we compared the simulations to the experiment directly on the image by calculating the squared saturation error in each voxel: $(S_{w\_exp}-S_{w\_mod})^2$. Cross-sections of these saturation error maps are are shown in Figure S5 in the Supporting Information S1. The blue color means the saturation error is very small, by contrast, red color indicates the saturation of model prediction has a large discrepancy in those pores compared with the experiment. It can be seen that the Pct-based model generally shows higher accuracy than the porosity-based model, especially unresolved regions at high capillary pressures.

The saturation error in certain open pores and in pores just above the image resolution is relatively large in the beginning of drainage in both models (pressure steps 1–3). To explain this, Figure 11 shows the pore radius distribution of water filled macropores and throats in the experiment and in the Pct-based model. We define the discrepancy of the filling state as the percentage of network elements that were occupied by a different fluid in the simulation than in the experiment (Bultreys et al., 2018). If more than half of the fluid within a single pore or throat was wetting phase, the pores or throats were considered to be wetting phase occupied, otherwise, they were classified as non-wetting phase filled. As expected, the non-wetting phase invaded large open pores and throats in the beginning, and almost all the brine within them was displaced before increasing to the fourth pressure.

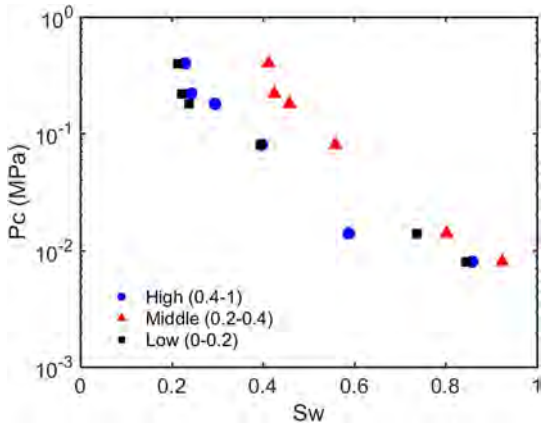

Figure 10. Average experimental saturation for the three micro-phase regions determined by the porosity-based sub-rock typing, for each capillary pressure step. These are the high (0.4–1), middle (0.2–0.4) and low (0–0.2) porosity regions respectively.

Similar to single-scale models (Bultreys et al., 2018), the pores and throats with intermediate size had the largest filling discrepancy. At the first drainage pressure, the occupancy for pores with large radius (>12 μm) had a close match. However, the simulation predicted that all small size macropores were wetting-filled while the experiment did not show this behavior. The throat filling error also reached 18.14% in this step. As shown in previous studies (Bultreys et al., 2018), the experimental fluid distribution and filling states at the pore scale are generally not fully reproducible, even in repeated experiments. Some of the pore-by-pore errors are likely caused by wrong invasion pressure predictions in throats that are only just above the resolution. These throats are treated as Darcy regions, which may yield inappropriate invasion pressure predictions. Furthermore, we only imaged the central part of the sample and the boundary conditions are therefore not exactly the same in the model and the experiment, which increased the pore-by-pore uncertainty of the simulation.

To quantitatively compare the saturation errors at each drainage step, we calculated the absolute average root mean square error (δ_{Abs}) and the volume weighted average root mean square error (δ_{VolWei}) of the models over the entire image:

$$\delta_{\mathrm{Abs}} = \sqrt{\frac{\sum (S_{\mathrm{w\_exp}} - S_{\mathrm{w\_mod}})^2}{N}} \tag{9}$$

$$\delta_{\mathrm{VolWei}} = \sqrt{\frac{\sum ((S_{\mathrm{w\_exp}} - S_{\mathrm{w\_mod}}) \cdot \varphi)^2}{N}} \tag{10}$$

where $S_{\mathrm{w\_exp}}$ and $S_{\mathrm{w\_mod}}$ are brine saturation of each voxel from experimental measurments and simulations respectively, φ is the corresponding porosity of each voxel, N is the total number of pore voxels.

Figure 12 indicates that the saturation error in the porosity-based model at high drainage pressures is significantly higher than that at low pressures, while the Pct-based model shows a smoother trend and lower errors, decreasing

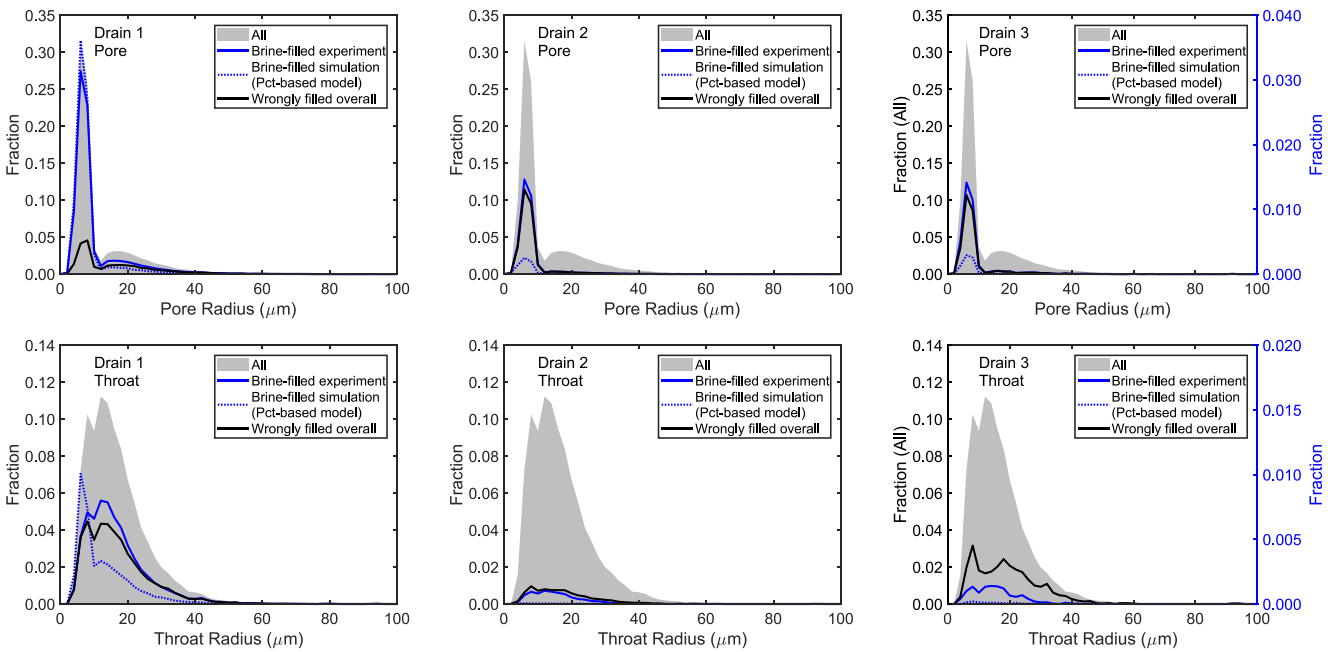

Figure 11. Water-filled open pore (top) and throat (bottom) size distribution after each drainage step.

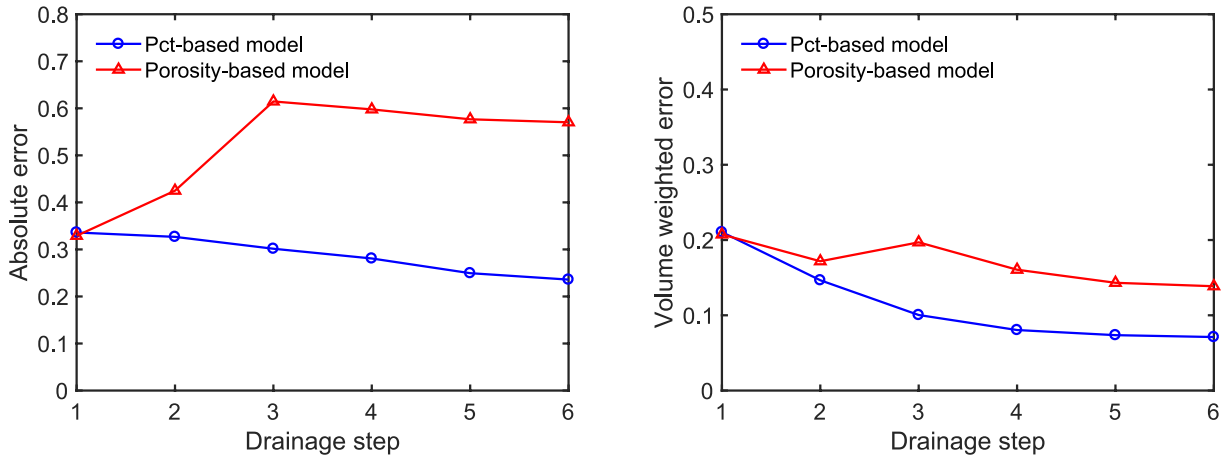

Figure 12. Absolute saturation error (left) and volume weighted saturation error (right) predicted by the two models.

from 0.34 to 0.26 with the increase of pressures. The high discrepancies in the first pressure steps may be related to the previously described mismatch in the macropores and throats of intermediate size. In the porosity-based model, which is tuned to an experimental P_c-curve, this can result in associated errors in the saturation distribution of the microporosity, as these errors compensate for the contribution of the macroporosity to the total saturation during the tuning step. The volume-weighted error in the porosity-based model is almost twice as high as in the Pct-based model in drainage steps 3–6.

4. Conclusions

In this work, we proposed a multi-scale PNM validation workflow using drainage experiments imaged with micro-CT, to study the factors that influence the uncertainty of pore-scale modeling and simulation. The differential imaging technique was used to quantify the porosity map and the saturation distribution during capillary-dominated drainage in an Estaillades limestone sample. A "classical" porosity-based and a novel invasion-capillary-pressure-based sub-rock typing methods were used to characterize the microporosity, followed by a multi-scale PNM extraction. The continuum scale properties and pore-scale multiphase distribution from the two models were then compared to experimental data.

We showed that the P_c-curves simulated by both models matched our image-based capillary pressure curve and an MICP curve of the rock type. The porosity-based model performed poorly in simulating multiphase fluid distribution at the pore-scale, while the novel Pct-based model significantly improved the prediction of pore filling states. This indicated that the multiphase transport behavior within sub-resolution pores was poorly correlated to the sub-voxel porosity. Further research should indicate if this is due to micropore geometry variations, due to capillary shielding (microporous regions with smaller pore sizes blocking access to larger pore sizes), or due to dynamic effects inside the microporosity, for example, inhomogeneous drainage due to extremely low brine conductivities that slow down the invasion to very long time scales. The methodology presented in this work was proven to be a promising approach in decreasing the uncertainty of pore-scale modeling. This will be checked for imbibition and more samples in our future study to make it possible to extend to other complex reservoir rocks modeling, to provide more insights on, for example, CO_2 sequestration and reservoir management.

Despite the improved results obtained with the Pct-based method, the determination of input petrophysical properties for microporous flow zones is still challenging and was shown to be a key factor affecting the reliability of the simulation. Furthermore, this current "best-fit" model is generated based on the fact that we have the full information of the drainage experiment. While this may be useful as a hybrid workflow to calculate properties that are difficult or impossible to measure in unsteady-state experiments, notably relative permeability, performing the experiment itself is time-consuming and complex. Therefore, a simplified workflow is needed to make the methodology more applicable for the real case, for instance, training a neural network to predict the Pct for each voxel based on a dry scan and a porosity map or other static information may be an option to avoid doing

flow experiment for every sample. Further work should also point out if the Pct-based rock-typing can serve as a baseline to develop more straightforward sub-rock typing methods.

Data Availability Statement

The data is made available on the Digital Rocks Portal (https://doi.org/10.17612/6RTT-5W16).

Acknowledgments
Veerle Cnudde and Arjen Mascini (Ghent University) are gratefully acknowledged for their advice and support during the experiment and the analysis. Shan Wang holds a PhD scholarship funded by the China Scholarship Council (CSC Grant 201906440157). Tom Bultreys is a post-doctoral fellow of the Research Foundation–Flanders (FWO) and acknowledges its support under grant 12X0919N. The special research fund of the Ghent University (BOF-UGent) is acknowledged for the financial support to the UGCT Centre of Expertise (BOF.EXP.2017.0007). Leonardo Ruspini would like to thank the Norwegian Research Council for partially supporting this research (grant 296093).

References

Alhashmi, Z., Blunt, M. J., & Bijeljic, B. (2015). Predictions of dynamic changes in reaction rates as a consequence of incomplete mixing using pore scale reactive transport modeling on images of porous media. *Journal of Contaminant Hydrology*, *179*, 171–181. https://doi.org/10.1016/j.jconhyd.2015.06.004

Alyafei, N., & Blunt, M. J. (2016). The effect of wettability on capillary trapping in carbonates. *Advances in Water Resources*, *90*, 36–50. https://doi.org/10.1016/j.advwatres.2016.02.001

Alyafei, N., Raeini, A. Q., Paluszny, A., & Blunt, M. J. (2015). A sensitivity study of the effect of image resolution on predicted petrophysical properties. *Transport in Porous Media*, *110*(1), 157–169. https://doi.org/10.1007/s11242-015-0563-0

Amid, A., Mignard, D., & Wilkinson, M. (2016). Seasonal storage of hydrogen in a depleted natural gas reservoir. *International Journal of Hydrogen Energy*, *41*(12), 5549–5558. https://doi.org/10.1016/j.ijhydene.2016.02.036

Arif, M., Lebedev, M., Barifcani, A., & Iglauer, S. (2017). CO_2 storage in carbonates: Wettability of calcite. *International Journal of Greenhouse Gas Control*, *62*, 113–121. https://doi.org/10.1016/j.ijggc.2017.04.014

Bauer, D., Youssef, S., Fleury, M., Bekri, S., Rosenberg, E., & Vizika, O. (2012). Improving the estimations of petrophysical transport behavior of carbonate rocks using a dual pore network approach combined with computed microtomography. *Transport in Porous Media*, *94*(2), 505–524. https://doi.org/10.1007/s11242-012-9941-z

Bera, B., Mitra, S. K., & Vick, D. (2011). Understanding the micro structure of Berea Sandstone by the simultaneous use of micro-computed tomography (micro-CT) and focused ion beam-scanning electron microscopy (FIB-SEM). *Micron*, *42*(5), 412–418. https://doi.org/10.1016/j.micron.2010.12.002

Blunt, M. J., Bijeljic, B., Dong, H., Gharbi, O., Iglauer, S., Mostaghimi, P., et al. (2013). Pore-scale imaging and modelling. *Advances in Water Resources*, *51*, 197–216. https://doi.org/10.1016/j.advwatres.2012.03.003

Boone, M. A., De Kock, T., Bultreys, T., De Schutter, G., Vontobel, P., Van Hoorebeke, L., & Cnudde, V. (2014). 3D mapping of water in oolithic limestone at atmospheric and vacuum saturation using X-ray micro-CT differential imaging. *Materials Characterization*, *97*, 150–160. https://doi.org/10.1016/j.matchar.2014.09.010

Bortone, I., Di Nardo, A., Di Natale, M., Erto, A., Musmarra, D., & Santonastaso, G. F. (2013). Remediation of an aquifer polluted with dissolved tetrachloroethylene by an array of wells filled with activated carbon. *Journal of Hazardous Materials*, *260*, 914–920. https://doi.org/10.1016/j.jhazmat.2013.06.050

Brooks, R. H., & Corey, A. T. (1964). *Hydraulic properties of porous media* (Doctoral dissertation). Colorado State University Libraries.

Brooks, R. H., & Corey, A. T. (1966). Properties of porous media affecting fluid flow. *Journal of the Irrigation and Drainage Division*, *92*(2), 61–88. https://doi.org/10.1061/JRCEA4.0000425

Bultreys, T., Boone, M. A., Boone, M. N., De Schryver, T., Masschaele, B., Van Hoorebeke, L., & Cnudde, V. (2016). Fast laboratory-based micro-computed tomography for pore-scale research: Illustrative experiments and perspectives on the future. *Advances in Water Resources*, *95*, 341–351. https://doi.org/10.1016/j.advwatres.2015.05.012

Bultreys, T., De Boever, W., & Cnudde, V. (2016). Imaging and image-based fluid transport modeling at the pore scale in geological materials: A practical introduction to the current state-of-the-art. *Earth-Science Reviews*, *155*, 93–128. https://doi.org/10.1016/j.earscirev.2016.02.001

Bultreys, T., Lin, Q., Gao, Y., Raeini, A. Q., AlRatrout, A., Bijeljic, B., & Blunt, M. J. (2018). Validation of model predictions of pore-scale fluid distributions during two-phase flow. *Physical Review E*, *97*(5), 053104. https://doi.org/10.1103/PhysRevE.97.053104

Bultreys, T., Singh, K., Raeini, A. Q., Ruspini, L. C., Øren, P. E., Berg, S., et al. (2020). Verifying pore network models of imbibition in rocks using time-resolved synchrotron imaging. *Water Resources Research*, *56*(6), e2019WR026587. https://doi.org/10.1029/2019WR026587

Bultreys, T., Stappen, J. V., Kock, T. D., Boever, W. D., Boone, M. A., Hoorebeke, L. V., & Cnudde, V. (2016). Investigating the relative permeability behavior of microporosity-rich carbonates and tight sandstones with multiscale pore network models. *Journal of Geophysical Research: Solid Earth*, *121*(11), 7929–7945. https://doi.org/10.1002/2016JB013328

Bultreys, T., Van Hoorebeke, L., & Cnudde, V. (2015). Multi-scale, micro-computed tomography-based pore network models to simulate drainage in heterogeneous rocks. *Advances in Water Resources*, *78*, 36–49. https://doi.org/10.1016/j.advwatres.2015.02.003

Carrillo, F. J., & Bourg, I. C. (2021). Modeling multiphase flow within and around deformable porous materials: A Darcy-Brinkman-Biot approach. *Water Resources Research*, *57*(2), e2020WR028734. https://doi.org/10.1029/2020wr028734

Ciobanu, C. L., Cook, N. J., Utsunomiya, S., Pring, A., & Green, L. (2011). Focussed ion beam–transmission electron microscopy applications in ore mineralogy: Bridging micro-and nanoscale observations. *Ore Geology Reviews*, *42*(1), 6–31. https://doi.org/10.1016/j.oregeorev.2011.06.012

Cnudde, V., & Boone, M. N. (2013). High-resolution X-ray computed tomography in geosciences: A review of the current technology and applications. *Earth-Science Reviews*, *123*, 1–17. https://doi.org/10.1016/j.earscirev.2013.04.003

De Boever, W., Derluyn, H., Van Loo, D., Van Hoorebeke, L., & Cnudde, V. (2015). Data-fusion of high resolution X-ray CT, SEM and EDS for 3D and pseudo-3D chemical and structural characterization of sandstone. *Micron*, *74*, 15–21. https://doi.org/10.1016/j.micron.2015.04.003

Devarapalli, R. S., Islam, A., Faisal, T. F., Sassi, M., & Jouiad, M. (2017). Micro-CT and FIB–SEM imaging and pore structure characterization of dolomite rock at multiple scales. *Arabian Journal of Geosciences*, *10*(16), 1–12. https://doi.org/10.1007/s12517-017-3120-z

Dierick, M., Van Loo, D., Masschaele, B., Van den Bulcke, J., Van Acker, J., Cnudde, V., & Van Hoorebeke, L. (2014). Recent micro-CT scanner developments at UGCT. *Nuclear Instruments and Methods in Physics Research Section B: Beam Interactions with Materials and Atoms*, *324*, 35–40. https://doi.org/10.1016/j.nimb.2013.10.051

Dong, H., & Blunt, M. J. (2009). Pore-network extraction from micro-computerized-tomography images. *Physical review E*, *80*(3), 036307. https://doi.org/10.1103/PhysRevE.80.036307

Gao, Y., Lin, Q., Bijeljic, B., & Blunt, M. J. (2017). X-ray microtomography of intermittency in multiphase flow at steady state using a differential imaging method. *Water Resources Research*, *53*(12), 10274–10292. https://doi.org/10.1002/2017WR021736

Gao, Y., Raeini, A. Q., Blunt, M. J., & Bijeljic, B. (2019). Pore occupancy, relative permeability and flow intermittency measurements using X-ray micro-tomography in a complex carbonate. *Advances in Water Resources*, *129*, 56–69. https://doi.org/10.1016/j.advwatres.2019.04.007

Gharbi, O., & Blunt, M. J. (2012). The impact of wettability and connectivity on relative permeability in carbonates: A pore network modeling analysis. *Water Resources Research*, *48*(12). https://doi.org/10.1029/2012WR011877

Ghous, A., Senden, T. J., Sok, R. M., Sheppard, A. P., Pinczewski, V. W., & Knackstedt, M. A. (2007). 3D characterisation of microporosity in carbonate cores. In *SPWLA Middle East regional symposium*. Society of Petrophysicists and Well-Log Analysts.

Guo, B., Ma, L., & Tchelepi, H. A. (2018). Image-based micro-continuum model for gas flow in organic-rich shale rock. *Advances in Water Resources*, *122*, 70–84. https://doi.org/10.1016/j.advwatres.2018.10.004

Han, M., Fleury, M., & Levitz, P. (2007). Effect of the pore structure on resistivity index curves. In *International symposium of the society of core analysts* (Vol. 34). Canada: Society of Core Analysts.

Jiang, Z., Van Dijke, M. I. J., Sorbie, K. S., & Couples, G. D. (2013). Representation of multiscale heterogeneity via multiscale pore networks. *Water Resources Research*, *49*(9), 5437–5449. https://doi.org/10.1002/wrcr.20304

Lin, Q., Al-Khulaifi, Y., Blunt, M. J., & Bijeljic, B. (2016). Quantification of sub-resolution porosity in carbonate rocks by applying high-salinity contrast brine using X-ray microtomography differential imaging. *Advances in Water Resources*, *96*, 306–322. https://doi.org/10.1016/j.advwatres.2016.08.002

Lin, Q., Bijeljic, B., Rieke, H., & Blunt, M. J. (2017). Visualization and quantification of capillary drainage in the pore space of laminated sandstone by a porous plate method using differential imaging X-ray microtomography. *Water Resources Research*, *53*(8), 7457–7468. https://doi.org/10.1002/2017WR021083

Lin, W., Li, X., Yang, Z., Manga, M., Fu, X., Xiong, S., et al. (2019). Multiscale digital porous rock reconstruction using template matching. *Water Resources Research*, *55*(8), 6911–6922. https://doi.org/10.1029/2019WR025219

Mason, G., & Morrow, N. R. (1991). Capillary behavior of a perfectly wetting liquid in irregular triangular tubes. *Journal of Colloid and Interface Science*, *141*(1), 262–274. https://doi.org/10.1016/0021-9797(91)90321-X

Mehmani, A., & Prodanović, M. (2014). The effect of microporosity on transport properties in porous media. *Advances in Water Resources*, *63*, 104–119. https://doi.org/10.1016/j.advwatres.2013.10.009

Mehmani, A., Verma, R., & Prodanović, M. (2020). Pore-scale modeling of carbonates. *Marine and Petroleum Geology*, *114*, 104141. https://doi.org/10.1016/j.marpetgeo.2019.104141

Menke, H., Gao, Y., Linden, S., & Andrew, M. (2019). Using nano-XRM and high-contrast imaging to inform micro-porosity permeability during Stokes-Brinkman single and two-phase flow simulations on micro-CT images. https://doi.org/10.31223/osf.io/ubg6p

Mouli-Castillo, J., Wilkinson, M., Mignard, D., McDermott, C., Haszeldine, R. S., & Shipton, Z. K. (2019). Inter-seasonal compressed-air energy storage using saline aquifers. *Nature Energy*, *4*(2), 131–139. https://doi.org/10.1038/s41560-018-0311-0

Nono, F., Bertin, H., & Hamon, G. (2014). An experimental investigation of the oil recovery in the transition zone of carbonate reservoirs taking into account wettability change. In *IPTC 2014: International petroleum technology conference* (pp. cp-395). European Association of Geoscientists & Engineers. https://doi.org/10.3997/2214-4609-pdb.395.IPTC-17640-MS

Olayiwola, S. O., & Dejam, M. (2019). A comprehensive review on interaction of nanoparticles with low salinity water and surfactant for enhanced oil recovery in sandstone and carbonate reservoirs. *Fuel*, *241*, 1045–1057. https://doi.org/10.1016/j.fuel.2018.12.122

Øren, P. E., Ruspini, L. C., Saadatfar, M., Sok, R. M., Knackstedt, M., & Herring, A. (2019). In-situ pore-scale imaging and image-based modelling of capillary trapping for geological storage of CO_2. *International Journal of Greenhouse Gas Control*, *87*, 34–43. https://doi.org/10.1016/j.ijggc.2019.04.017

Pan, C., Hilpert, M., & Miller, C. T. (2004). Lattice-Boltzmann simulation of two-phase flow in porous media. *Water Resources Research*, *40*(1). https://doi.org/10.1029/2003WR002120

Prodanović, M., Mehmani, A., & Sheppard, A. P. (2015). Imaged-based multiscale network modelling of microporosity in carbonates. *Geological Society, London, Special Publications*, *406*(1), 95–113. https://doi.org/10.1144/SP406.9

Purcell, W. R. (1949). Capillary pressures-their measurement using mercury and the calculation of permeability therefrom. *Journal of Petroleum Technology*, *1*(2), 39–48. https://doi.org/10.2118/949039-g

Raeini, A. Q., Blunt, M. J., & Bijeljic, B. (2012). Modelling two-phase flow in porous media at the pore scale using the volume-of-fluid method. *Journal of Computational Physics*, *231*(17), 5653–5668. https://doi.org/10.1016/j.jcp.2012.04.011

Ruspini, L. C., Farokhpoor, R., & Øren, P. E. (2017). Pore-scale modeling of capillary trapping in water-wet porous media: A new cooperative pore-body filling model. *Advances in Water Resources*, *108*, 1–14. https://doi.org/10.1016/j.advwatres.2017.07.008

Ruspini, L. C., Lindkvist, G., Bakke, S., Alberts, L., Carnerup, A. M., & Øren, P. E. (2016). A multi-scale imaging and modeling workflow for tight rocks. In *SPE low perm symposium*. Society of Petroleum Engineers.

Ruspini, L. C., Øren, P. E., Berg, S., Masalmeh, S., Bultreys, T., Taberner, C., et al. (2021). Multiscale digital rock analysis for complex rocks. *Transport in Porous Media*, *139*(2), 301–325. https://doi.org/10.1007/s11242-021-01667-2

Scheibe, T. D., Perkins, W. A., Richmond, M. C., McKinley, M. I., Romero-Gomez, P. D., Oostrom, M., et al. (2015). Pore-scale and multiscale numerical simulation of flow and transport in a laboratory-scale column. *Water Resources Research*, *51*(2), 1023–1035. https://doi.org/10.1002/2014wr015959

Shanley, K. W., Cluff, R. M., & Robinson, J. W. (2004). Factors controlling prolific gas production from low-permeability sandstone reservoirs: Implications for resource assessment, prospect development, and risk analysis. *AAPG Bulletin*, *88*(8), 1083–1121. https://doi.org/10.1306/03250403051

Wang, J., Song, H., & Wang, Y. (2020). Investigation on the micro-flow mechanism of enhanced oil recovery by low-salinity water flooding in carbonate reservoir. *Fuel*, *266*, 117156. https://doi.org/10.1016/j.fuel.2020.117156

Wirth, R. (2009). Focused ion beam (FIB) combined with SEM and TEM: Advanced analytical tools for studies of chemical composition, microstructure and crystal structure in geomaterials on a nanometre scale. *Chemical Geology*, *261*(3–4), 217–229. https://doi.org/10.1016/j.chemgeo.2008.05.019

Youssef, S., Han, M., Bauer, D., Rosenberg, E., Bekri, S., Fleury, M., & Vizika, O. (2008). High resolution μ-CT combined to numerical models to assess electrical properties of bimodal carbonates. In *International symposium of core analysts* (pp. 1–12).